1-1-2022

Packable and Readily Deployable Tightly Coupled Dipole Array (TCDA) With Integrated Planar Balun

Md Rakibul Islam
Florida International University

Maxence Carvalho
Florida International University

Satheesh Bojja Venkatakrishnan
Florida International University

John L. Volakis
Florida International University

Packable and Readily Deployable Tightly Coupled Dipole Array (TCDA) With Integrated Planar Balun

MD RAKIBUL ISLAM (Member, IEEE), **MAXENCE CARVALHO** (Member, IEEE),
SATHEESH BOJJA VENKATAKRISHNAN (Senior Member, IEEE),
AND JOHN L. VOLAKIS (Life Fellow, IEEE)

Department of Electrical Engineering, Florida International University, Miami, FL 33174, USA

CORRESPONDING AUTHOR: M. R. ISLAM (e-mail: misla077@fiu.edu)

ABSTRACT To overcome the limited payload dedicated to onboard antennas for CubeSat/SmallSat applications, this paper presents a novel, foldable, dual-polarized Tightly Coupled Dipole Array (TCDA). In comparison to previous vertical feeds used for TCDAs, this array integrates a planar microstrip balun feed to enable foldability. The proposed array attains 5.4:1 (0.6-3.20 GHz) impedance bandwidth with VSWR < 3 at broadside and scans down to 45° at all azimuth planes. Notably, a substrate-integrated in-plane folding mechanism based on Lamina Emergent Torsion (LET) joints is employed to achieve foldability coupled with a simple fabrication process. The average simulated radiation efficiency was 95% across the band. A 5 × 8 prototype array was fabricated and tested to verify the finite array's foldability, bandwidth, and gain performance. This prototype achieves 80% one-dimensional size reduction, yielding 60% overall volume reduction. Consequently, the array prototype can be folded and stowed in a compact volume of 1.4U (25 cm× 7.2 cm× 9 cm).

INDEX TERMS Foldable antenna array, origami, phased arrays, satellite antennas, tightly coupled dipole array (TCDA).

I. INTRODUCTION

THE DEVELOPMENT of wideband, high-gain antennas plays a key role for several space technologies, including remote sensing/imaging, inter-satellite links (ISLs), and high data rate ground-satellite communications. Additionally, modern space and satellite communications require broadband coverage and high reliability with reduced size, weight, power, and cost (SWaP-C). Furthermore, for next generations satellite applications, phased arrays can increase gain and mitigate interference with beamsteering capability. Consequently, space technologies are eyeing conformal and thin arrays operating across a wide bandwidth. However, the implementation of traditional antenna arrays is restricted by limited launch volume [1]. Notably, for space applications the arrays must be compactly stowed to accommodate the limited allocated storage [2].

The focus of this paper is the development of low complexity folding, and the realization of wideband operation

across wide scans [1], [2], [3]. As is known, ultra-wideband (UWB) phased arrays are often constrained by the size-bandwidth-efficiency-scanning metrics [4]. One such UWB phased array (with over 10:1 BW) is the Vivaldi array. But Vivaldi arrays are heavy and not readily foldable [5], [6], [7], [8].

On the other hand, tightly coupled dipole arrays (TCDA) are known for their low profile, very large contiguous bandwidth, and high cross-polarization isolation [4], [9], [10], [11], [12], [13], [14], [15]. However, so far, existing TCDAs employed vertically oriented balun feeds [4], [14], [15]. Hence, previous TCDA designs are not easily packaged for folding and deployment.

Recently, a rigid-flexible TCDA (RF-TCDA) design demonstrated foldability of a TCDA using a combination of a flexible Kapton substrate with rigid FR4 [16]. This RF-TCDA design uses a tapered transmission line balun at the dipole layer to achieve foldability. However,
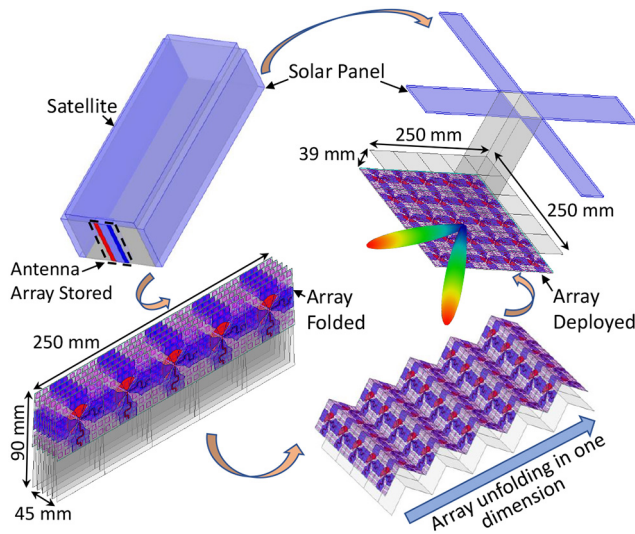
FIGURE 1. States of the CubeSat deployment for a 5 × 5 TCDA. This TCDA achieves 80% size reduction in one direction implying a 60% overall volume reduction.

TABLE 1. Final design parameters of the TCDA unit cell in Fig. 2.

Parameters	Dimensions (mm)
$D_x = a = b$	50
W_{dipole}	17.4
d	39
w_{FSS}	4.13
g_{FSS}	3
t	1.9
L_t	14
W_t	1.7
W_s	1.9
W_b	2

the employed parallel-strip tapered transmission line balun in [16] prevented dual-polarization operation and introduced higher cross-polarization.

To enable foldability of the spaceborne antennas, numerous techniques were presented in the literature. In [17], [18], mesh-surfaced reflector antennas were presented to achieve the foldability and deployability of the spaceborne antennas. However, this kind of antenna suffers from undesired surface roughness, leading to poor gain performance. In [3], [19], flexible membrane-based deployable antenna arrays were presented. The latter were very lightweight and compact for space applications. But their deployment process is complex and often causes damage to the membrane causing creases at the folding joints.

A rigid foldable technique was proposed in [2], [16], [20], where the rigid parts of the antenna were joined with a flexible substrate material (Kapton Pyralux) at the folding locations. This approach is challenging for fabrication, particularly when a continuous metal connection is needed across the flexible substrate. In comparison to the abovementioned approaches, an in-plane Lamina Emergent Torsion (LET) joint was considered in [21], [22]. Monolithic fabrication of this joint from a rigid substrate simplifies the fabrication process while still ensuring the rigidity of the design.

This paper addresses the existing issues associated with the design and fabrication of spaceborne, foldable, UWB antenna array and their feed. Specifically, a foldable tightly coupled dipole array (TCDA) is presented that employs a planar microstrip-to-slotline balun feed on the same plane as the antenna array. This is done by printing the microstrip balun on the flip side of the dipole substrate, thus preventing the feed from causing undesirable cross-polarization. Another notable advantage of this design is the co-phase-centered dual-polarization operation which can not be realized using

the traditional egg-crate TCDA configuration. Notably, a substrate-integrated in-plane folding mechanism based on LET joint is employed to achieve foldability, which requires a simple and low-cost fabrication process. Consequently, the dipole and ground plane layers can be folded to significantly reduce array volume by 60%. The presented TCDA delivers a 5.4:1 (0.6 GHz to 3.2 GHz) bandwidth at broadside and scans down to 45° off-broadside at all azimuth planes. It is noted that the array retains its performance even after several folding and unfolding cycles. Also, the total height of the TCDA is quite thin, with only a thickness of $\lambda_{low}/14$ (where λ_{low} being the wavelength at the lowest frequency of operation).

This paper is organized as follows. Section II details the design of the proposed TCDA. The prototype fabrication and measurements are given in Section III. Conclusions and future work plans are presented in Section IV.

II. ARRAY DESIGN AND SIMULATION

The proposed dual-polarized array is shown in Fig. 2. This model was designed and simulated using Periodic Boundary Condition (PBC) set-up using commercial software Ansys HFSS [23]. As depicted in Fig. 2, the unit cell is comprised of two main sections: the array layer and ground plane layer. These layers are separated by a distance of $d = 39\ mm$. This distance was carefully optimized to achieve a ground plane reactive impedance of $Z_{GP} = j\eta_0\tan(\beta d)$, where η_0 is the free-space impedance, and β is the propagation constant [10]. Hence, the ultra wide-band operation of the TCDA is achieved by counterbalancing the ground plane inductance with the capacitive coupling between the neighboring array elements. The array stack-up comprises four metal layers. Top to bottom these are: 1) frequency selective surface (FSS) superstrate, 2) microstrip feed for horizontal (H) polarization, 3) microstrip feed for vertical polarization (V), and 4) dipole layer. The key design detail and layer stack diagram of the TCDA unit cell is shown in Fig. 2. The final design parameters of the unit cell are given in Table 1.

Below, Sections II-A–II-D discuss the design guidelines of each section for the proposed dual-polarized TCDA.
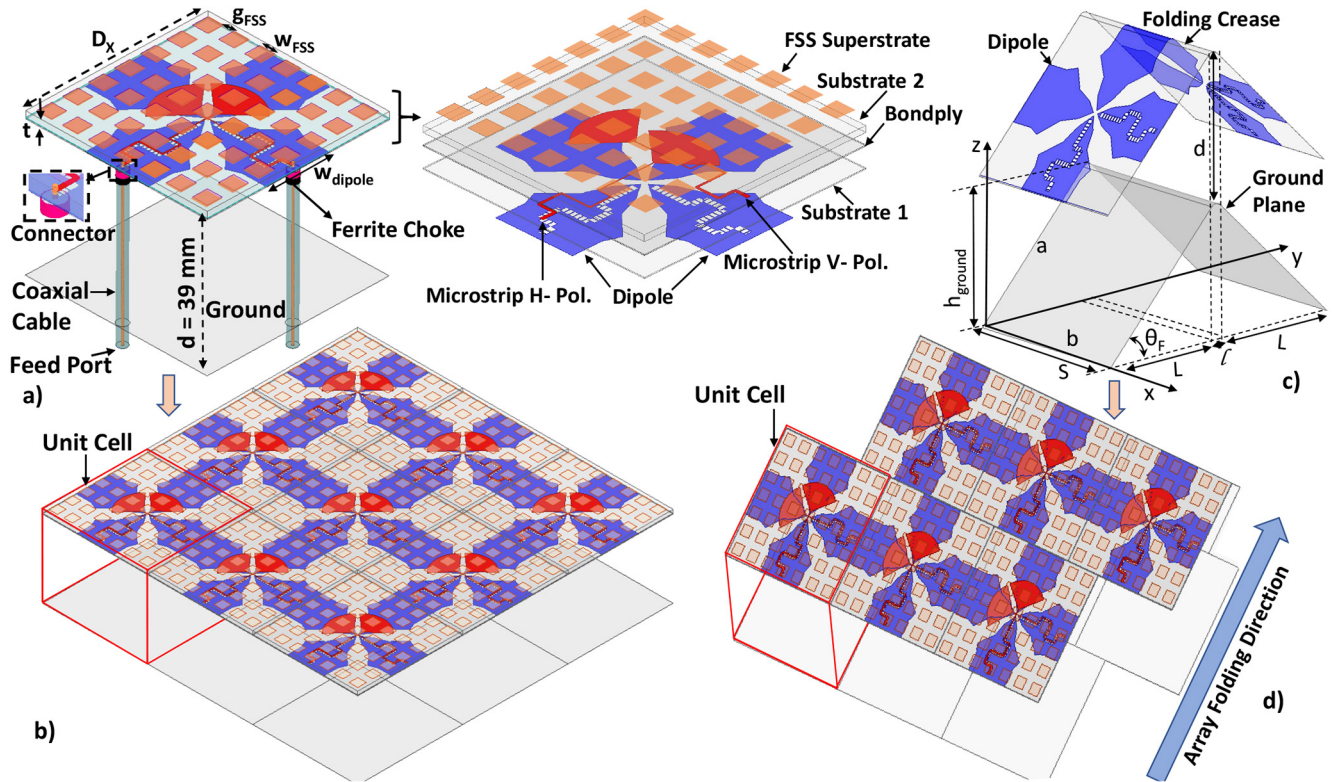
FIGURE 2. Proposed rigid-foldable TCDA details. a) Unit cell in isometric view, b) 3 × 3 array of the unit cell, c) Folding of the unit cell, d) 3 × 3 array showing one-dimensional folding.
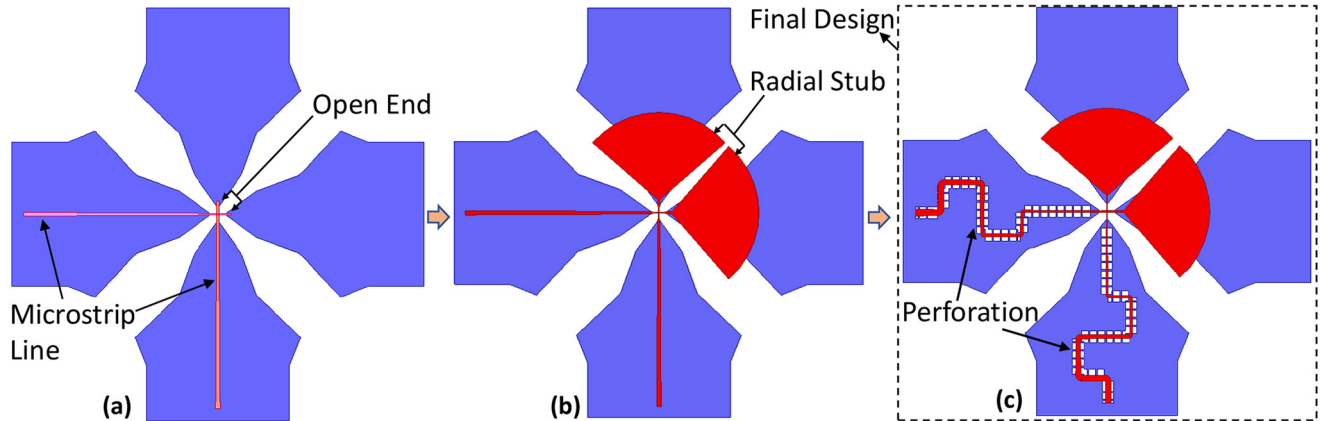

FIGURE 3. Evolution of the feed design throughout the design process. a) Straight microstrip line with open end termination, b) Straight microstrip line with radial stub termination, c) Meandered microstrip line with radial stub termination and perforation at the ground.

A. ORIGAMI-BASED FOLDABLE UNIT CELL DESIGN

The unit cell design is depicted in Figs. 2 and 3. The dipoles are etched on the bottom-most layer of the two-layer stack-up. Rogers RT/duroid 5880 ($\epsilon_r = 2.2$) was used as the substrate and the dipoles were designed for a maximum separation of $\lambda_{high}/2$, where λ_{high} is the wavelength at the highest frequency of operation viz. $f_{high} = 3.2$ GHz. Doing so, scanning at low angles is achieved without grating lobes. Notably, bow-tie-shaped dipoles were chosen for improved bandwidth. The dipoles were designed and optimized to have

a narrow tip at the feed to accommodate dual polarization concentrically. As noted, no overlapping pads were used between neighboring (dipole) elements since the focus was folding not the bandwidth beyond 7:1 [4], [24], [25]. This folding approach facilitated the use of LET joints placed at the dipole edges.

To enable folding, the unit cell was placed on an origami-based lattice as proposed in [16]. Referring to Fig. 2(c), θ_F is the folding angle relative to the flat plane. Specifically, $\theta_F = 0°$ refers to the unfolded (flat) case, and $\theta_F = 90°$

refers to the fully folded case. From geometry, the unit cell lattice parameters can be expressed as follows:

$$h_{\text{ground}} = a\sin\theta_F \qquad (1)$$

$$L = a\cos\theta_F \qquad (2)$$

$$S = b \qquad (3)$$

In the above, a and b are the side lengths of the unit cell substrate. Therefore, the total volume of the unit cell at any folding state is given by: Volume $= S\,[\,(L+l)\,]\,[\,(h_{\text{ground}}+d)\,]$.

B. PLANAR MICROSTRIP BALUN FEED DESIGN

A planar microstrip-to-slotline balun was used for feeding the dipoles, as depicted in Figs. 2 and 3. This feeding facilitated the transition between the unbalanced microstrip and the inherently balanced slotline. This type of microstrip-to-slotline balun feed has been previously used for archimedean spirals [26], [27], [28]. Notably, the antenna arm serves as a ground plane for the microstrip line [29]. As depicted in Fig. 2, the center pin of the 50 Ω connector excites the microstrip line at the end of each dipole arm. Subsequently, the microstrip line travels toward the center of the dipole and transitions to a balanced slot. At the center of the dipole, the microstrip crosses the dipole gap to terminate at a radial stub.

The strategic positioning of the radial stub improves impedance matching. Additionally, perforations were added across the dipoles arm. These perforations control the capacitance between the microstrip and the ground plane (dipole arms) to achieve improved impedance transition. To further improve impedance matching, both the microstrip feed line and the perforations were meandered and tapered along the length of the dipole [13]. The evolution of the aforementioned feed design is depicted in Fig. 3.

C. FREQUENCY SELECTIVE SURFACE (FSS) SUPERSTRATE

In earlier TCDA designs, dielectric slabs were used to improve scanning performance [10]. However, these dielectric slabs added weight while providing low-angle scanning. To circumvent dielectric superstrate drawbacks, vertical FSS superstrates were presented in [4], [13], [30]. Instead, here we consider a planar FSS superstrate to enable the folding of the antenna array. Also, by optimizing the dipole to FSS superstrate height (t), width (w_{FSS}), and spacing (g_{FSS}) the scanning impedance is improved. That is, the FSS superstrate is tuned with the rest of the array to improve scanning across the operating frequency range. The final dimensions of the FSS superstrate are given in Table 1.

D. LAMINA EMERGENT TORSION (LET) JOINT

The proposed TCDA incorporated a compliant joint mechanism (surrogate hinge) using lamina emergent torsion (LET)
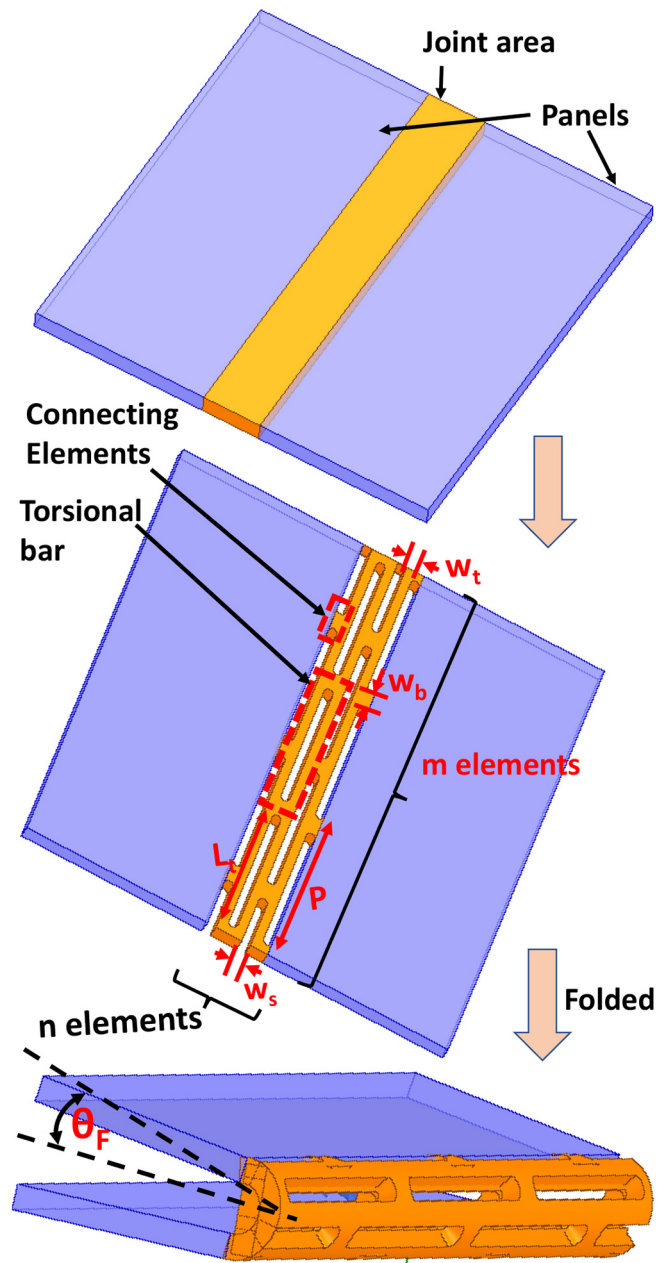

FIGURE 4. LET joint folding mechanism is shown with design parameters.

joint to achieve folding and self-deployability. Unlike the conventional hinge mechanisms, the LET joint achieves the required movement of folding through deflection of the material at the joint area. Thus, with the combination of bending and twisting, the LET joints provides rotational motion out of the plane to accommodate folding [31]. Notably, flexibility at the joints is achieved by reducing the stiffness through optimization of the LET joint cuts/slots. As depicted in Fig. 4, the LET cuts/slots are milled on a monolithic substrate to build out the LET joint. These LET joints employ parallel and series arrangements of torsional bars to form an $m\times n$ array. Here, m and n refer to the number of elements in parallel and series, respectively. The stiffness of a torsional
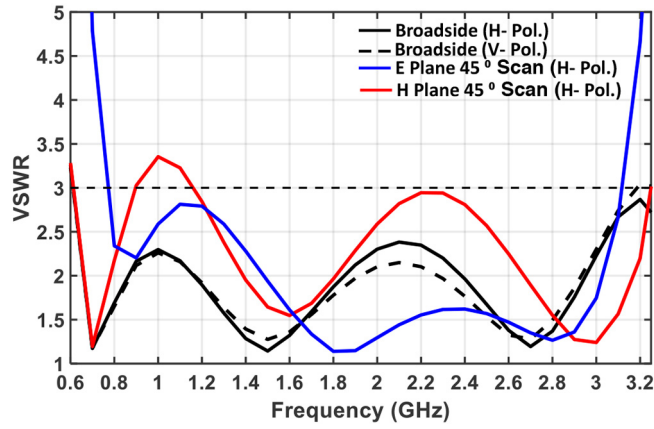
FIGURE 5. Simulated active VSWR of the infinite array (includes the effect of LET cuts) in the E- and H- planes while scanning at $\theta = 0°$ and $\theta = 45°$.
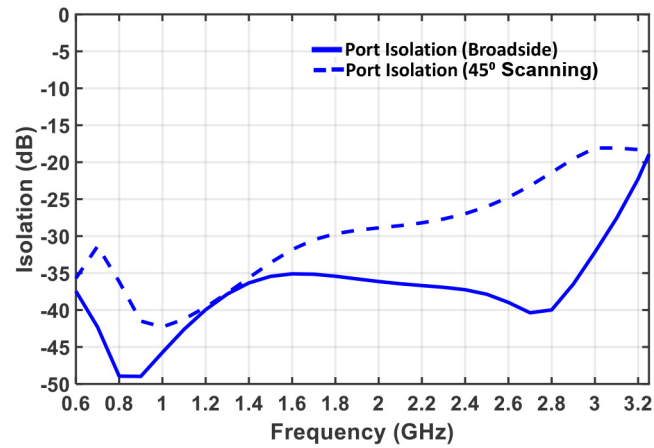

FIGURE 6. Simulated port-to-port isolation between orthogonal polarization.

bar or element is given [21], [32] as

$$k_{unit} = \frac{2k_b k_t}{k_t + 2k_b} \qquad (4)$$

In the above, k_b and k_t refer to the bending and torsional stiffnesses, respectively.

Further, for a joint comprised of m parallel and n series elements, the overall stiffness of the hinges along the folding direction can be expressed as

$$k_{array} = \frac{m}{n} k_{unit} \qquad (5)$$

This expression shows that the overall stiffness of the hinge decrease with n, viz., the number of torsional bar connected in series.

Overall, optimal LET joint folding can be achieved through the combination of LET joint cut optimization and befitting materials properties, e.g., tensile modulus, E, Poisson's ratio, ν. As such, LET joint optimization and the material selections are discussed in the fabrication section.

E. INFINITE ARRAY SIMULATIONS
Using the optimized unit cell element in a periodic array, an infinite array simulation was carried out. As depicted in
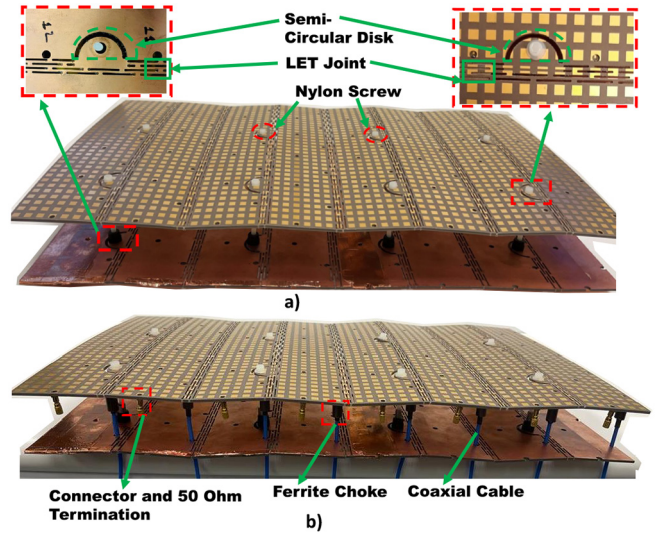

FIGURE 7. The fabricated 5 × 8 antenna array prototype with LET joints. a) Slanted view delineating folding features, b) Side view depicting RF cable assemblies.

Fig. 5, the dual-polarized array provides VSWR < 3 across 0.6 GHz to 3.20 GHz for the horizontal (H- Pol.) and vertical polarizations (V- Pol.) at broadside. Overall, the VSWR for both polarizations are similar across the majority of the band except for the frequencies at the edges of the band. Henceforth, taking advantage of the symmetry of the design, and since the H-pol has the high VSWR, only simulation and measurements for this polarization will be discussed for the rest of the paper. When scanning in both E- and H- plane down to 45°, the unit cell still maintains VSWR< 3 across 0.6 GHz to 3.2 GHz. As expected, higher VSWR is observed in the H-plane due to the $1/\cos\theta$ impedance variation [33]. Notably, the employed planar FSS superstrate of square patches serves to retain VSWR<3 during scanning. However, VSWR for scanning in both E- and H- planes can be further improved by increasing the thickness/gap, t (see in Fig. 2) between the dipole and FSS superstrate.

Simulated port-to-port isolation for the two polarizations (H- and V- pol.) are given in Fig. 6, showing > 30 dB isolation, on average, between the ports at broadside. At 45° scanning, the isolation is > 25 dB, on average. The simulated radiation efficiency, on average, was achieved to be ∼ 95% across the operating frequency band.

III. PROTOTYPE FABRICATION AND MEASUREMENT
A. FABRICATED PROTOTYPE
A 5 × 8 dual-polarized array prototype was fabricated to verify the design. Specifically, the dipoles were printed on the bottom layer of a Rogers RT/duroid 5880 ($\epsilon_r = 2.2$) substrate (thickness 10 mils). Notably, for the H- polarization, the microstrip feed line was printed on the top of the same 10 mil substrate. Further, the microstrip feed line for the other polarization was printed at the bottom layer of a separate Rogers RT/duroid 5880 substrate 60 mils thick and placed above the 10 mils dipole substrate. Both substrate
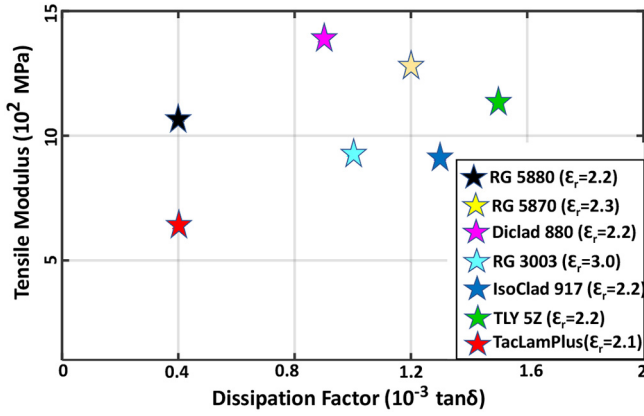
FIGURE 8. Material selection based on elasticity and dissipation factor (tan δ) properties.

layers were bonded together using Rogers 2929 bondply ($\epsilon_r = 2.9$). Finally, the FSS elements were printed on top of the 60 mils substrate. The complete stack-up of the antenna array layers are given in Fig. 2(a).

The ground plane layer of the antenna array was printed on a separate Rogers RT/duroid 5880 substrate (thickness = 60 mils). Holes were also drilled in the ground plane. These holes were used to insert the coaxial cables for feeding the microstrip lines. Notably, a ferrite choke was used near the feeding point to prevent backward current density leaks at the outer conductor of the coaxial cable, and suppress common mode radiation. Further, to ensure the quality of the fabricated prototype, commercially printed PCB manufacturing guidelines were followed throughout the entire design process. That is, minimum metal trace widths and a conductor separation of 0.15 mm (6 mils) were maintained.

B. LET JOINTS OPTIMIZATION AND MINIMIZING THEIR EFFECT ON ANTENNA'S RF PERFORMANCE

A key aspect of the presented design is its robustness along with folding flexibility at the joint using LET cuts. From Fig. 8, it can be observed that Rogers RT/duroid 5880 and Rogers DiClad 880 substrates were a good fit to achieve the required robustness of the design with high tensile modulus [34]. Eventually, the low dissipation factor ($\tan\delta = 9 \times 10^{-4}$) of Rogers RT/duroid 5880 substrate makes it attractive for low-loss RF applications.

Optimization of the LET cut/slot array was carried out to minimize the Von Mises stress (resultant stress of torsional and bending stress) at the LET joint. This was done while minimizing the footprint of the joint area. We note that the torsional stress is proportional to W_t and inversely proportional to L_t. Also, bending stress is inversely proportional to W_b [31], [32]. We remark that the minimum constraint for W_t was the fabrication tolerance and the robustness of the torsional bars for multiple folding cycles. An additional constraint relates to maximum L_t and W_b was the width of the dipole end, W_{dipole} (see Fig. 9) to ensure that the LET cut does not split the dipole arm. Furthermore, the stiffness
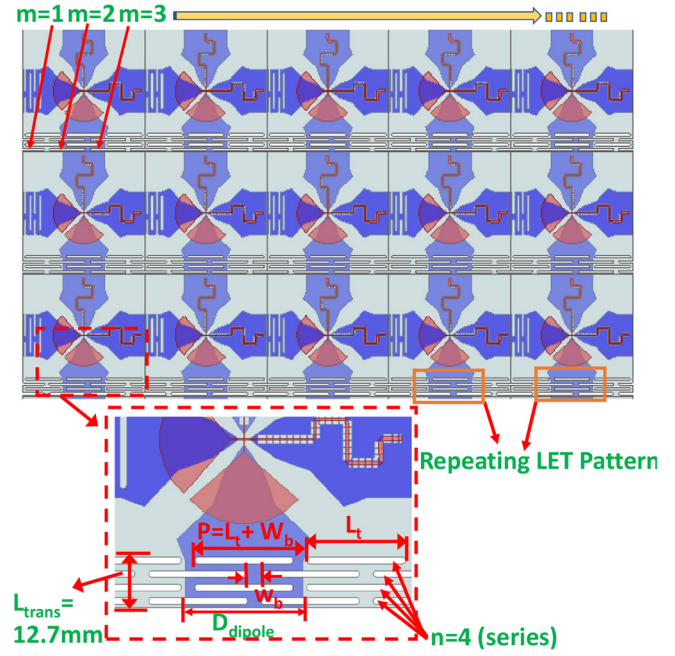

FIGURE 9. Optimized LET cuts depicted on dipole arm.

of the joint is inversely proportional to the number of series torsional bars, n. However, a larger n increases the LET joint's footprint. As such, the number of series elements, n, should be chosen to optimize stiffness with a smaller LET joint footprint. Notably, the maximum Von Misses stress at the joint can be expressed as [32]

$$\sigma_{\max} = \frac{2k_t k_b \theta_{F,max}}{n(k_t + 2k_b)} \sqrt{\left(\frac{9}{w_b^2 t^4}\right) + \left(\frac{3}{4Q^2}\right)} \quad (6)$$

In the above, t is the total thickness of the substrate, $\theta_{F,max}$ is the maximum folding angle, and Q refers to a geometry-dependent parameter, $Q = \frac{w_t^2 t^2}{3w_t + 1.8t}$. Further, the total length of the LET joint in the transverse direction, L_{trans} (perpendicular to the joint axis) is given by

$$L_{trans} = n(2w_s + 2w_t) + w_s \quad (7)$$

With the above relations in mind, we adopt the following cost function for optimizing the LET joint [35]

$$Cost = \sqrt{w_{i1}\left(\frac{\sigma_{\max}}{\sigma_{target}} - 1\right)^2 + w_{i2}\left(\frac{L_{trans}}{L_{target}} - 1\right)^2} \quad (8)$$

In the above, $\sigma_{target} = 840$ MPa, and $L_{target} = 13$ mm are the desired stress and LET joint transverse lengths, respectively. Also, w_{i1} and w_{i2} are normalized weights with $w_{i1} + w_{i2} = 1$ and w_{i1} & $w_{i2} > 0$.

Genetic algorithm was used to optimize the parameters and minimize the cost function in (8). The optimized parameters of the LET joint are given in Table 1, with the Von Mises stresses at the LET joint being 850 MPa. The optimized LET joint allows for 360° bending about its axis of
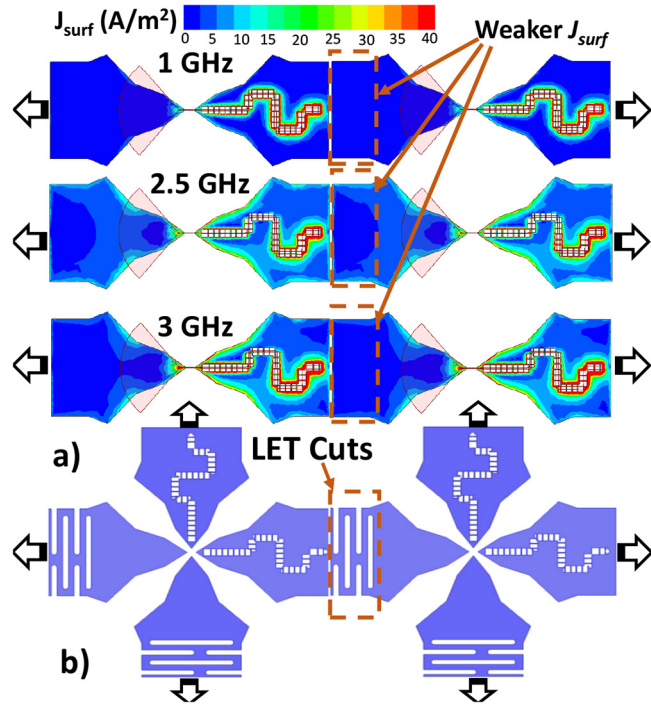
FIGURE 10. a) Color map of the dipole surface current density for a single polarization at three different frequencies across the operating band, b) LET joint cuts/slots and their placement between the dipole arms.

FIGURE 11. Effect of LET joint cuts on antenna performance while scanning at $\theta = 0°$ and $\theta = 45°$.

symmetry. Concurrently, this folding approach achieved high compactness.

The effect of the LET joint cuts was examined to assess their impact on the antenna array's RF performance. Surface current density (J_{surf}) is depicted for a single polarization in Fig. 10, where the arrows shows the array expansion. As depicted in Fig. 10, the dipole currents near the coaxial feed have a stronger J_{surf} and this was to be expected. Consequently, the LET cuts were placed at the end of the dipole arms and opposite to the feed location where J_{surf} is comparatively weaker. Simulated VSWR of the infinite array with and without LET joint cuts are depicted in Fig. 11. It was observed that the LET joint cuts have minimal effect on the antenna's performance at broadside and while scanning at 45° off-broadside.

C. ARRAY FOLDING MECHANISM

As depicted in Fig. 12, the antenna array and ground layers are kept together and at a constant distance using nylon screws. Further, a semi-circular disk was introduced (see Fig. 7) to facilitate the folding of the array along with the nylon screw. This disk can rotate 180° up/down with respect to the horizontal plane for complete folding of the antenna array. The folding states of the antenna array are depicted in Fig. 12. It is remarked that the radius of the semi-circular disk (see Fig. 12) limits the maximum folding angle to $\theta_{F,max} = 80°$. At this folding angle, the TCDA achieves an 80% size reduction along one dimension, implying an overall volume reduction of 60%. That is, this 5×8 array prototype
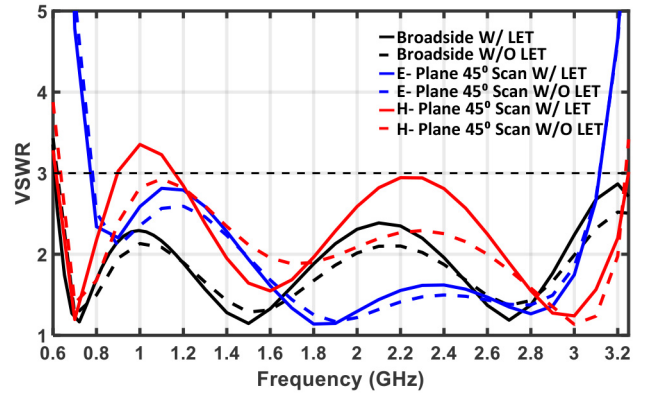
of 40 cm $\times$ 25 cm $\times$ 3.9 cm in volume is reduced to 1.4 U at its maximum folding state. However, depending on the RF connectors and cable assembly choices, the maximum folding angle may need to be relaxed by 5° to 10°. Specifically, when SMPM connectors are used, the maximum folding should be relaxed by 7° (see Fig. 13).

The robustness of the proposed foldable design was tested through a fatigue test for numerous folding cycles and antenna's RF performance was also measured for those cycles. For this test, only the center element port was excited while other neighboring ports were terminated with matched load. The results of the VSWR measurements are depicted in Fig. 14. It was observed that the array's RF performance was not affected significantly after the 200 folding cycles.

D. ACTIVE IMPEDANCE MEASUREMENTS

The fabricated array in Fig. 7 was used for measuring the active impedance using a Keysight N5222B Vector Network Analyzer (VNA). To compute the impedance of the desired element (center element), the mutual coupling with neighboring ones was measured, and combined with the measured reflection co-efficient of that element. While measuring the element impedance, non-excited ports were terminated with a 50 Ω load at the microstrip balun input. The active reflection coefficient at the desired element (p,q) was evaluated as follows [15], [36]:

$$\Gamma_{pq}(\theta, \phi) = \sum_{m=1}^{M} \sum_{n=1}^{N} V_{mn} S_{mn,pq} e^{-jD([m-p]u+[n-q]v)} \quad (9)$$

In the above, $u = k \sin\theta \cos\phi$ and $v = k \sin\theta \sin\phi$, k defines the free-space wavenumber, and $S_{mn,pq}$ refer to the S-parameter between the mn^{th} and pq^{th} elements of the array. As usual, M, N and D are the number of elements along the x and y directions and the array lattice spacing.

During measurements, the edge effect due to the finite size of the array were also taken into account in calculating the active reflection coefficient. Notably, due to reduced element to element coupling, the edge elements of a finite array
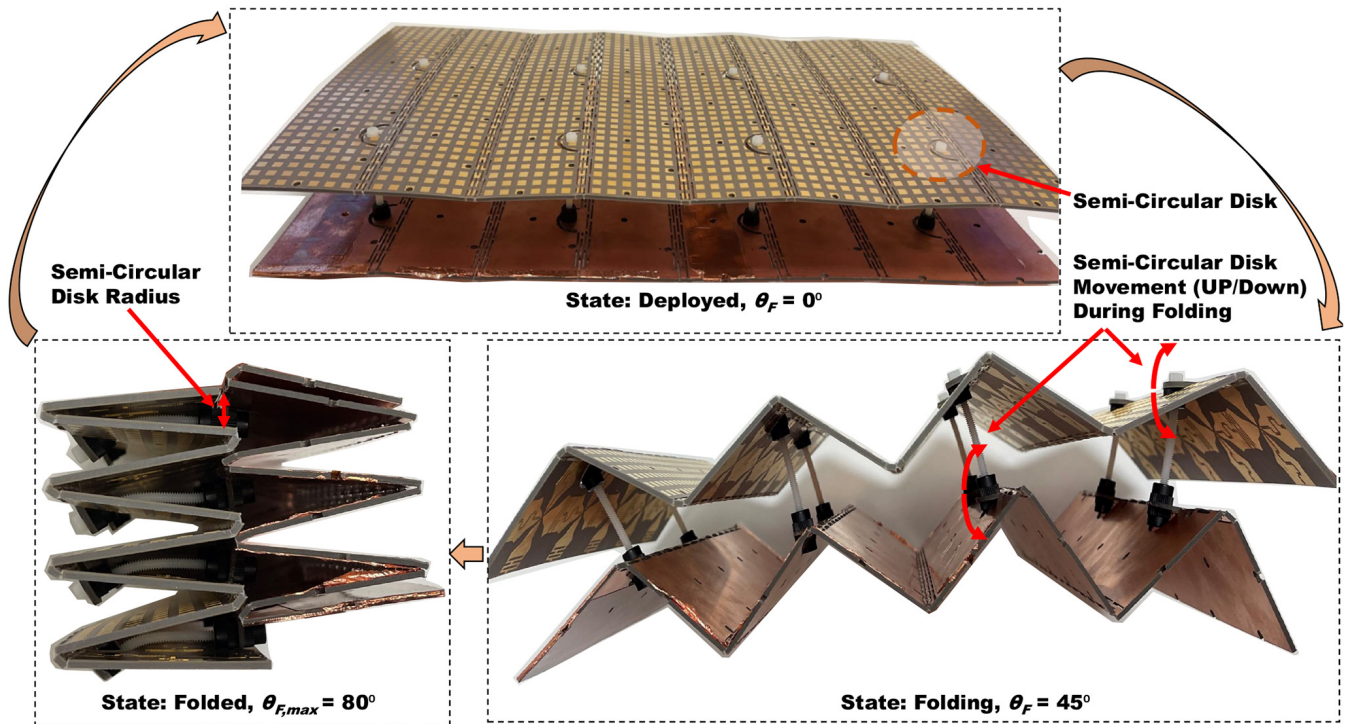
FIGURE 12. Folding process of the TCDA (without RF connectors) at different states (where $\theta_F = 0°$ is deployed and $\theta_{F,max} = 80°$ is folded state).
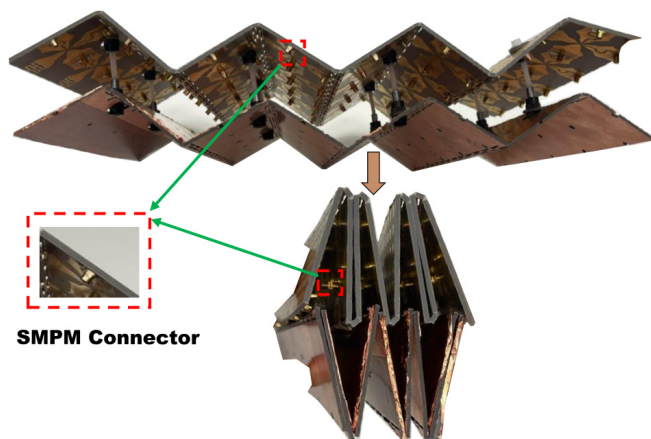

FIGURE 13. Array folding depicted with SMPM connector.
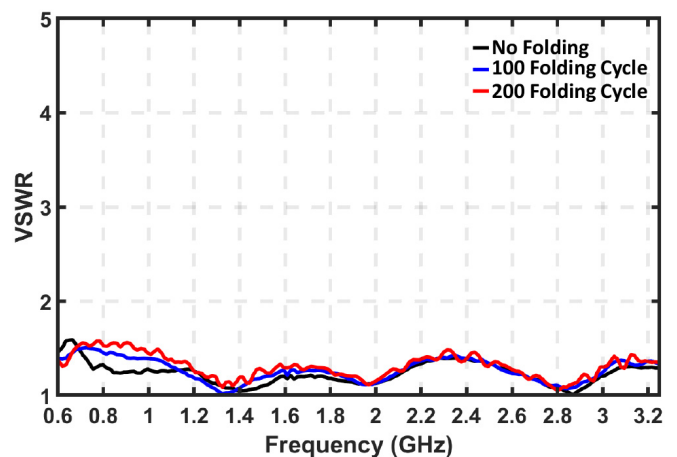

FIGURE 14. VSWR measurement of the center element during fatigue test.

have slightly different impedance characteristics than the center element [37]. Therefore, to achieve optimum matching across the 5×8 array, power tapering was adopted [37], [38], [39]. Specifically, a cosine amplitude tapering was implemented as depicted in Fig. 15, represented by V_{mn} in (9).

Using the amplitude tapering, the active VSWR of the center array element of the fabricated prototype was measured at broadside and at $45°$ off-broadside scanning. Semi-infinite array simulations were also carried out using the set-up discussed in [4], [16] to assess the effects of amplitude excitation tapering. The simulation model

depicted in Fig. 16 employs eight array elements in the x-direction and uses periodic boundary conditions (PBC) along the y-direction. Also, the finite element mesh absorbing boundaries were placed at $\lambda_{low}/4$ distance from the array perimeter.

The measured results are given in Figs. 17 and 18 for the finite array vs the semi-infinite array and infinite array simulations. As seen, the simulations and measurements are in good agreement, giving a VSWR < 3 from 0.6 to 3.2 GHz at broadside. Specifically, the semi-infinite array simulation corroborates measurements at the lower band.
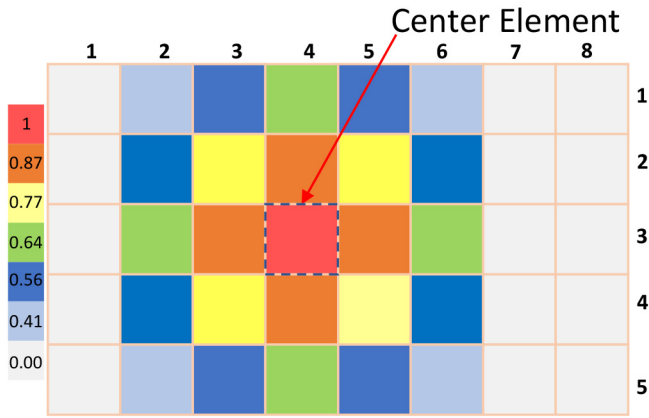
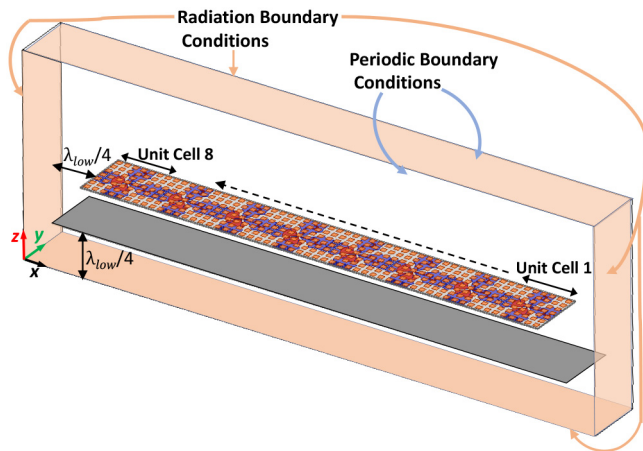FIGURE 15. Cosine amplitude tapering of the excitation.

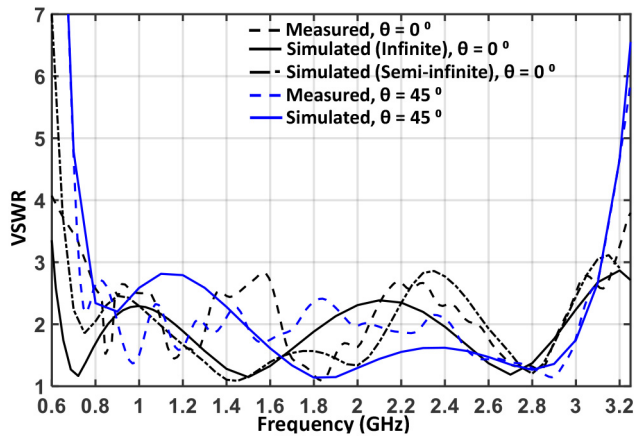FIGURE 16. Simulation setup for an 8 × 1 semi-infinite array with periodic boundary condition in one direction.

FIGURE 17. Measured vs. simulated active VSWR of the center element of the TCDA at $\theta = 0°$ and at $\theta = 45°$ in the E- plane.

It is also observed that the active VSWR while scanning agrees well with simulations. It is remarked that the measured performance of the proposed array, specifically at the low band, could be improved by fabricating a larger array.
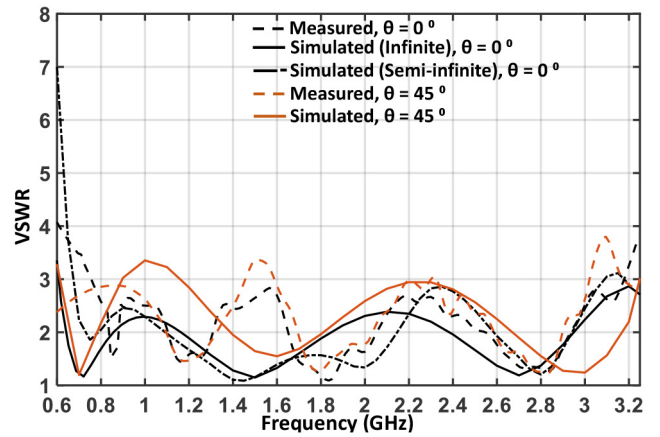

FIGURE 18. Measured vs. simulated active VSWR of the center element of the TCDA at $\theta = 0°$ and at $\theta = 45°$ in the H- plane.

FIGURE 19. Far-field gain measurement set up with a high gain LPDA as the reference antenna.

E. FAR FIELD MEASUREMENTS

Gain measurements were performed using a near-field anechoic chamber from 0.65 GHz to 3.2 GHz. At frequency range from 0.6 to 0.65 GHz, outdoor gain measurements were carried out using an LPDA to set the reference gain. Further, to avoid nearby and ground reflections, the measurements were conducted in an open field using an elevated antenna as depicted in Fig. 19. The separation of the antenna and the transmitter were set to 3 m with the antennas placed at a height of 3 m from the ground. The measured broadside gain for both the co- and cross-polarizations is given in Fig. 20 from 0.6 to 3.2 GHz. It is compared to the theoretical aperture gain = $4\pi A/\lambda^2$. As seen, the measured and simulated gain are in close agreement with some losses at the high band attributed to the ferrite choke [40] placed at the coaxial cable feed. Notably, the measured average cross-polarization level is approximately below 20 dB. This cross-polarization measurement can be improved further using careful fabrication and a better-suited reference antenna.

Gain patterns for both E- and H-planes are depicted in Fig. 21 and Fig. 22, respectively. It is observed that finite array pattern measurements are in good agreement with
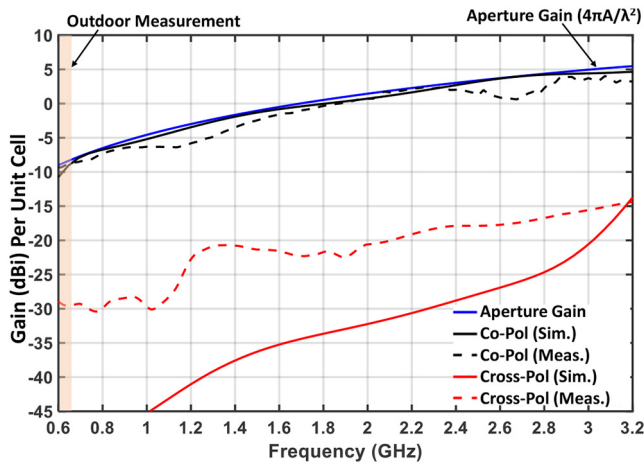
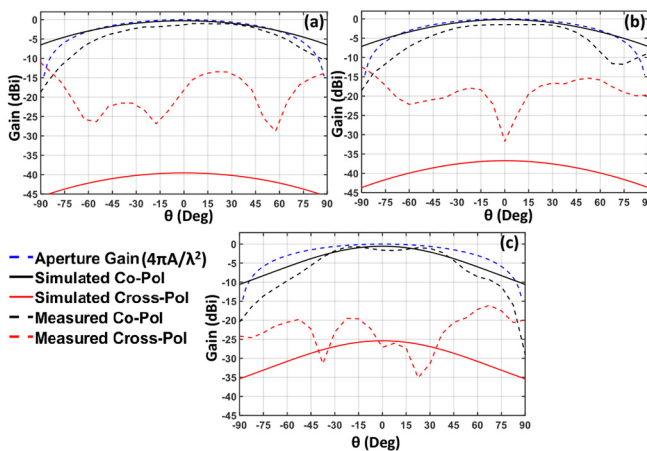**FIGURE 20.** Measured gain of the center element vs. simulation at broadside.

FIGURE 21. Measured and simulated normalized gain patterns per unit cell in the E-plane at a) 700 MHz, b) 1500 MHz, and c) 3000 MHz. On average, more than 20 dB polarization purity is achieved up to $\theta = 45°$.
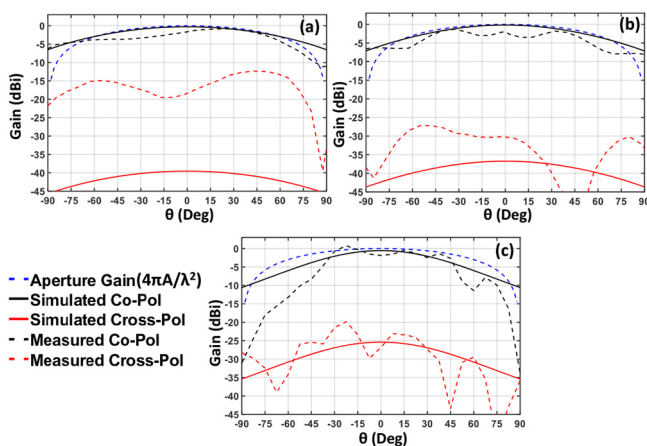

FIGURE 22. Measured and simulated normalized gain patterns per unit cell in the H-plane at a) 700 MHz, b) 1500 MHz, and c) 3000 MHz. On average, more than 20 dB polarization purity is achieved up to $\theta = 45°$.

simulations. Minor distinctions observed between E- and H- plane patterns resulted from the unequal number of elements along E- and H- plane directions.

IV. CONCLUSION

This paper focused on presenting a foldable and readily deployable TCDA for low-angle scanning. Specifically, to achieve foldability with dual-polarization operation, a planar microstrip-to-slotline balun feed was adopted. The presented array operates across 0.6-3.2 GHz with dual-linear polarization and scanning down to $\theta = 45°$. The array provided average simulated radiation efficiency of 95% across the operating band.

A key aspect of the design is the array's foldability using LET joint as the in-plane folding mechanism, build-out monolithically on the substrate. This approach simplified the fabrication as well as folding and deployment. A 5×8 prototype was fabricated and measured to verify folding and array gain and bandwidth performance. Folding of the array leads to an overall volume reduction of 60%. The measured data at broadside and at $\theta = 45°$ from broadside showed close agreement to simulations. The presented one-dimensional foldable array with the planar feed can be implemented for two-dimensional folding like Miura-Ori for further volume reduction.

ACKNOWLEDGMENT

REFERENCES

[1] P. Warren, J. W. Steinbeck, R. J. Minelli, and C. Mueller, "Large, deployable S-band antenna for a 6U Cubesat," in *Proc. AIAA/USU Conf. Small Satellites*, 2015, pp. 1–7.

[2] W. F. Moulder, R. N. Das, A. C. Maccabe, L. A. Bowen, E. M. Thompson, and P. J. Bell, "Rigid-flexible antenna array (RFAA) for lightweight deployable apertures," in *Proc. 14th Eur. Conf. Antennas Propag. (EuCAP)*, 2020, pp. 1–5.

[3] F. Zhang, G.-M. Yang, Y.-Q. Jin, F. Peng, and J. Mo, "Space-borne deployable P-band dual-circular-polarization flexible antenna array," *IEEE Antennas Wireless Propag. Lett.*, vol. 16, pp. 2529–2533, 2017.

[4] J. Zhong, A. Johnson, E. A. Alwan, and J. L. Volakis, "Dual-linear polarized phased array with 9:1 bandwidth and 60° scanning off broadside," *IEEE Trans. Antennas Propag.*, vol. 67, no. 3, pp. 1996–2001, Mar. 2019.

[5] D. Schaubert, S. Kasturi, A. O. Boryssenko, and W. M. Elsallal, "Vivaldi antenna arrays for wide bandwidth and electronic scanning," in *Proc. 2nd Eur. Conf. Antennas Propag. (EuCAP)*, 2007, pp. 1–6.

[6] J. T. Logan, R. W. Kindt, and M. N. Vouvakis, "Low cross-polarization Vivaldi arrays," *IEEE Trans. Antennas Propag.*, vol. 66, no. 4, pp. 1827–1837, Apr. 2018.

[7] J. T. Logan, R. W. Kindt, and M. N. Vouvakis, "A 1.2–12 GHz sliced notch antenna array," *IEEE Trans. Antennas Propag.*, vol. 66, no. 4, pp. 1818–1826, Apr. 2018.

[8] M. W. Elsallal and J. C. Mather, "An ultra-thin, decade (10:1) bandwidth, modular 'BAVA' array with low cross-polarization," in *Proc. IEEE Int. Symp. Antennas Propag. (APSURSI)*, 2011, pp. 1980–1983.

[9] W. F. Moulder, K. Sertel, and J. L. Volakis, "Ultrawideband superstrate-enhanced substrate-loaded array with integrated feed," *IEEE Trans. Antennas Propag.*, vol. 61, no. 11, pp. 5802–5807, Nov. 2013.

[10] W. F. Moulder, K. Sertel, and J. L. Volakis, "Superstrate-enhanced ultrawideband tightly coupled array with resistive FSS," *IEEE Trans. Antennas Propag.*, vol. 60, no. 9, pp. 4166–4172, Sep. 2012.

[11] M. H. Novak, F. A. Miranda, and J. L. Volakis, "Ultra-wideband phased array for millimeter-wave ISM and 5G bands, realized in PCB," *IEEE Trans. Antennas Propag.*, vol. 66, no. 12, pp. 6930–6938, Dec. 2018.

[12] M. H. Novak and J. L. Volakis, "Ultrawideband antennas for multiband satellite communications at UHF–ku frequencies," *IEEE Trans. Antennas Propag.*, vol. 63, no. 4, pp. 1334–1341, Apr. 2015.

[13] E. Yetisir, N. Ghalichechian, and J. L. Volakis, "Ultrawideband array with 70° scanning using FSS superstrate," *IEEE Trans. Antennas Propag.*, vol. 64, no. 10, pp. 4256–4265, Oct. 2016.

[14] A. D. Johnson, J. Zhong, S. B. Venkatakrishnan, E. A. Alwan, and J. L. Volakis, "Phased array with low-angle scanning and 46:1 bandwidth," *IEEE Trans. Antennas Propag.*, vol. 68, no. 12, pp. 7833–7841, Dec. 2020.

[15] M. Carvalho, A. D. Johnson, E. A. Alwan, and J. L. Volakis, "Semi-resistive approach for tightly coupled dipole array bandwidth enhancement," *IEEE Open J. Antennas Propag.*, vol. 2, pp. 110–117, 2021.

[16] M. Carvalho and J. L. Volakis, "Deployable rigid-flexible tightly coupled dipole array (RF-TCDA)," *IEEE Open J. Antennas Propag.*, vol. 2, pp. 1184–1193, 2021.

[17] N. Chahat, J. Sauder, R. Hodges, M. Thomson, Y. R. Samii, and E. Peral, "Ka-band high-gain mesh deployable reflector antenna enabling the first radar in a CubeSat: RainCube," in *Proc. 10th Eur. Conf. Antennas Propag. (EuCAP)*, 2016, pp. 1–4.

[18] C. S. MacGillivray, "Miniature high gain antenna for CubeSats," in *Proc. CubeSat Develop. Workshop*, 2011, pp. 1–11.

[19] A. Moussessian et al., "An active membrane phased array radar," in *IEEE MTT-S Int. Microw. Symp. Dig.*, 2005, pp. 1711–1714.

[20] M. Carvalho and J. L. Volakis, "Performance of partially deployed spaceborne ultra-wideband Miura-Ori apertures," *IEEE Open J. Antennas Propag.*, vol. 2, pp. 718–725, 2021.

[21] M. Hamza, C. L. Zekios, and S. V. Georgakopoulos, "A thick origami reconfigurable and packable patch array with enhanced beam steering," *IEEE Trans. Antennas Propag.*, vol. 68, no. 5, pp. 3653–3663, May 2020.

[22] M. Hwang, G. Kim, S. Kim, and N. S. Jeong, "Origami-inspired radiation pattern and shape reconfigurable dipole array antenna at C-band for CubeSat applications," *IEEE Trans. Antennas Propag.*, vol. 69, no. 5, pp. 2697–2705, May 2021.

[23] "Ansys-HFSS." Accessed: Jun. 30, 2022. [Online]. Available: https://www.ansoft.com/products/hf/hfss/

[24] J. P. Doane, K. Sertel, and J. L. Volakis, "Matching bandwidth limits for arrays backed by a conducting ground plane," *IEEE Trans. Antennas Propag.*, vol. 61, no. 5, pp. 2511–2518, May 2013.

[25] J. P. Doane, K. Sertel, and J. L. Volakis, "A wideband, wide scanning tightly coupled dipole array with integrated balun (TCDA-IB)," *IEEE Trans. Antennas Propag.*, vol. 61, no. 9, pp. 4538–4548, Sep. 2013.

[26] M. W. Nurnberger and J. L. Volakis, "A new planar feed for slot spiral antennas," *IEEE Trans. Antennas Propag.*, vol. 44, no. 1, pp. 130–131, Jan. 1996.

[27] J. A. Kasemodel, C.-C. Chen, I. J. Gupta, and J. L. Volakis, "Miniature continuous coverage antenna array for GNSS receivers," *IEEE Antennas Wireless Propag. Lett.*, vol. 7, pp. 592–595, 2008.

[28] J. A. Kasemodel and J. L. Volakis, "A planar dual linear-polarized antenna with integrated balun," *IEEE Antennas Wireless Propag. Lett.*, vol. 9, pp. 787–790, 2010.

[29] H. Lee, M. M. Tentzeris, and J. Geiger, "Flexible spiral antenna with microstrip tapered infinite balun for wearable applications," in *Proc. IEEE Int. Symp. Antennas Propag.*, 2012, pp. 1–2.

[30] A. O. Bah, P.-Y. Qin, R. W. Ziolkowski, Y. J. Guo, and T. S. Bird, "A wideband low-profile tightly coupled antenna array with a very high figure of merit," *IEEE Trans. Antennas Propag.*, vol. 67, no. 4, pp. 2332–2343, Apr. 2019.

[31] J. O. Jacobsen, G. Chen, L. L. Howell, and S. P. Magleby, "Lamina emergent torsional (LET) joint," *Mech. Mach. Theory*, vol. 44, no. 11, pp. 2098–2109, 2009.

[32] B. P. D. Figueiredo, "Developing new classes of thick-origami-based mechanisms: Conceal-and-reveal motion and folding printed circuit boards," Ph.D. dissertation, Dept. Mech. Eng., Brigham Young Univ., Provo, UT, USA, 2017.

[33] H. Wheeler, "Simple relations derived from a phased array made of an infinite current sheet," in *Proc. Antennas Propag. Soc. Int. Symp.*, vol. 2, 1964, pp. 157–160.

[34] "ACS-product-selector-guide-and-standard-thicknesses-and-tolerances.pdf." Rogers. Accessed: Jun. 10, 2022. [Online]. Available: https://www.rogerscorp.com

[35] J. Zhao, D. Psychoudakis, C.-C. Chen, and J. L. Volakis, "Design optimization of a low-profile UWB body-of-revolution monopole antenna," *IEEE Trans. Antennas Propag.*, vol. 60, no. 12, pp. 5578–5586, Dec. 2012.

[36] N. Amitay, V. Galindo, and C. P. Wu, *Theory and Analysis of Phased Array Antennas*. New York, NY, USA: Wiley, 1972.

[37] I. Tzanidis, K. Sertel, and J. L. Volakis, "Characteristic excitation taper for ultrawideband tightly coupled antenna arrays," *IEEE Trans. Antennas Propag.*, vol. 60, no. 4, pp. 1777–1784, Apr. 2012.

[38] H. Holter and H. Steyskal, "On the size requirement for finite phased-array models," *IEEE Trans. Antennas Propag.*, vol. 50, no. 6, pp. 836–840, Jun. 2002.

[39] D. Pozar, "Analysis of finite phased arrays of printed dipoles," *IEEE Trans. Antennas Propag.*, vol. AP-33, no. 10, pp. 1045–1053, Oct. 1985.

[40] "Ferrite EMI cable cores—Laird." Accessed: Sep. 26, 2022. [Online]. Available: https://www.laird.com/products/inductive-components-emc-components-and-ferrite-cores/ferrite-cable-cores

MD RAKIBUL ISLAM (Member, IEEE) was born in Nilphamari, Bangladesh, in 1990. He received the bachelor's degree in electrical engineering from the Rajshahi University of Engineering and Technology, Rajshahi, Bangladesh, in 2013, and the M.Sc. degree in electrical engineering from Georgia Southern University, USA, in 2017. He is currently pursuing the Ph.D. degree with RFCOM Lab, Florida International University, Miami, FL, USA. His current research interests include reconfigurable antennas and ultra-wideband phased arrays for mmWave/sub-6 GHz 5G bands. He was the recipient of the Student Fellowship Travel Grant Award at the U.S. National Committee for the International Union of Radio Science in 2018 and 2021.

MAXENCE CARVALHO (Member, IEEE) was born in Clermont–Ferrand, France, in 1994. He received the M.Sc. degree in aeronautical and spatial telecommunications from the l'École National de l'Aviation Civile, Toulouse, France, in 2018. He is currently pursuing the Ph.D. degree with RFCOM Lab, Florida International University, Miami, FL, USA. His current research interests include ultra-wideband arrays, millimeter-wave antennas for imaging applications, and reconfigurable antennas. He was the Honorable Mention Award Recipient in the Student Paper Competition at the 2021 National Radio Science Meeting.

SATHEESH BOJJA VENKATAKRISHNAN (Senior Member, IEEE) was born in Tiruchirappalli, India, in 1987. He received the bachelor's degree in electronics and communication engineering from the National Institute of Technology, Tiruchirappalli, in 2009, and the M.S. and Ph.D. degrees in electrical engineering from The Ohio State University, Columbus, OH, USA, in 2017. He was a Scientist with DRDO, India, from 2009 to 2013, working on the development and implementation of active electronic steerable antennas. He is currently a Research Assistant Professor of Electrical and Computer Engineering with Florida International University. He is also working on Simultaneous Transmit and Receive System to improve the spectral efficiency. His current research includes receiver design for communication circuits, RF systems, and digital signal processing using FPGAs. He was a recipient of the IEEE Electromagnetic Theory Symposium Young Scientist Award in 2019. He won the 2nd Prize in International Union of Radio Science General Assembly and Scientific Symposium Student Paper Competition held at Montreal, Canada, in August 2017. He also received the Honorable Mention in the Student Paper Competition at the IEEE Antenna and Propagation Symposium in 2015 and 2016, and the Student Fellowship Travel Grant Award at the U.S. National Committee for the International Union of Radio Science in 2016 and 2017. He has been a Phi Kappa Phi Member since 2015.

JOHN L. VOLAKIS (Life Fellow, IEEE) was born in Chios, Greece, in 13 May 1956, and immigrated to USA, in 1973. He received the B.E. degree (*summa cum laude*) from Youngstown State University, Youngstown, OH, USA, in 1978, and the M.Sc. and Ph.D. degrees from The Ohio State University, Columbus, OH, USA, in 1979, and 1982, respectively. He started his career with Rockwell International North American Aircraft Operations from 1982 to 1984, currently Boeing. In 1984, he was appointed as an Assistant Professor with the University of Michigan, Ann Arbor, MI, USA, and became a Full Professor in 1994. He also served as the Director of Radiation Laboratory from 1998 to 2000. From January 2003 to August 2017, he was the Roy and Lois Chope Chair Professor of Engineering with The Ohio State University and served as the Director of the ElectroScience Laboratory from 2003 to 2016. Since August 2017, he has been the Dean of the College of Engineering and Computing and a Professor with the Electrical and Computer Engineering, Florida International University. His publications include eight books, over 440 journal papers and 900 conference papers, 30 book chapters, and 30 patents/disclosures. Among his coauthored books are: *Approximate Boundary Conditions in Electromagnetics* in 1995; *Finite Element Methods for Electromagnetics* in 1998; *Antenna Engineering Handbook* (4th and 5th ed.) in 2007 and 2019; *Small Antennas* in 2010; and *Integral Equation Methods for Electromagnetics* in 2011. Over the years, he carried out research in computational methods, antennas, wireless communications and propagation, electromagnetic compatibility and interference, design optimization, RF materials, multiphysics engineering, millimeter waves, terahertz, and medical sensing. He has graduated/mentored 97 doctoral students/postdoctoral students with 43 of them receiving Best Paper Awards at conferences. Among his Awards are: The University of Michigan College of Engineering Research Excellence Award in 1993, the Scott Award from the Ohio State University College of Engineering for Outstanding Academic Achievement in 2011, the IEEE AP Society C-T. Tai Teaching Excellence Award in 2011, the IEEE Henning Mentoring Award in 2013, the IEEE Antennas and Propagation Distinguished Achievement Award in 2014, The Ohio State University Distinguished Scholar Award in 2016, and The Ohio State University ElectroScience Laboratory George Sinclair Award in 2017, and the URSI Booker Gold Medal in 2020. His service to Professional Societies include: The 2004 President of the IEEE Antennas and Propagation Society in 2004, the Chair of USNC/URSI Commission B from 2015 to 2017, twice the General Chair of the IEEE Antennas and Propagation Symposium, the IEEE APS Distinguished Lecturer, the IEEE APS Fellows Committee Chair, the IEEE-wide Fellows committee Member and an Associate Editor of several journals. He was listed by ISI among the top 250 most referenced authors in 2004. He is a Fellow of the Advanced Computational Electromagnetics Society, the American Association for the Advancement of Science, and the National Academy of Inventors in 2021.